Intercomparison of 3D Pore-scale Flow and Solute Transport Simulation Methods

Xiaofan Yang[a], Yashar Mehmani[b], William A. Perkins[a], Martin Schönherr[c], Andrea Pasquali[c], Colin Clark[f], Kyungjoo Kim[d], Mauro Perego[d], Michael L. Parks[d], Matthew T. Balhoff[e], Marshall C. Richmond[a], Martin Geier[c], Manfred Krafczyk[c], Li-Shi Luo[h], Alexandre M. Tartakovsky[a], C. Larrabee Winter[f,g], Timothy D. Scheibe[a,*]

[a]*Pacific Northwest National Laboratory, PO Box 999, MS K9-36, Richland, WA 99352*
[b]*Stanford University, School of Earth, Energy and Environmental Sciences, 397 Panama Mall, Mitchell Building 101, Stanford, CA 94305-2210*
[c]*Institute for Computational Modelling in Civil Engineering, Technische Universität Braunschweig, Pockelsstr. 3, 38106 Braunschweig, Germany*
[d]*Sandia National Laboratories, PO Box 5800, Albuquerque, NM 87185*
[e]*University of Texas at Austin, Department of Petroleum and Geosystems Engineering, 200 E. Dean Keeton St., Stop C0300, Austin TX 78712-1585*
[f]*University of Arizona, Program in Applied Mathematics, Tucson, AZ 85721*
[g]*University of Arizona, Department of Hydrology and Water Resources, Tucson, AZ 85721*
[h]*Old Dominion University, Department of Mathematics and Statistics, Engineering I& Computational Science Building, 4700 Elkhorn Ave., Norfolk VA 23529*

Abstract

Multiple numerical approaches have been developed to simulate porous media fluid flow and solute transport at the pore scale. These include methods that 1) explicitly model the three-dimensional geometry of pore spaces and 2) those that conceptualize the pore space as a topologically consistent set of stylized pore bodies and pore throats. In previous work we validated a model of class 1, based on direct numerical simulation using computational fluid dynamics (CFD) codes, against magnetic resonance velocimetry (MRV) measurements of pore-scale velocities. Here we expand that validation to include additional models of class 1 based on the immersed-boundary methd (IMB), lattice Boltzmann method (LBM), smoothed particle hydrodynamics (SPH), as well as a model of class 2 (a pore-

*Corresponding author
Email address: tim.scheibe@pnnl.gov (Timothy D. Scheibe)

network model or PNM). The PNM approach used in the current study was recently improved and demonstrated to accurately simulate solute transport in a two-dimensional experiment. While the PNM approach is computationally much less demanding than direct numerical simulation methods, the effect of conceptualizing complex three-dimensional pore geometries on solute transport in the manner of PNMs has not been fully determined. We apply all four approaches (CFD, LBM, SPH and PNM) to simulate pore-scale velocity distributions and nonreactive solute transport, and intercompare the model results with previously reported experimental observations. Experimental observations are limited to measured pore-scale velocities, so solute transport comparisons are made only among the various models. Comparisons are drawn both in terms of macroscopic variables (e.g., permeability, solute breakthrough curves) and microscopic variables (e.g., local velocities and concentrations).

Keywords: Pore-scale modeling, porous media flow, validation, computational fluid dynamics, lattice Boltzmann method, pore-network method, immersed-boundary method

---

1. Introduction

Flow and transport processes in porous media have been intensively studied over decades because of their importance in many industrial, biological, and environmental applications [6]. Pore space geometry and topology are key factors that influence flow and transport phenomena through porous media, but the complexity of natural pore geometries renders it challenging to both measure and simulate pore-scale flow and transport processes. So mathematical models are often developed and applied under different conditions [7]. Because of the availability of increasingly more powerful computional resources, pore-scale modeling has become an important tool for studying complex flow and transport processes and relating them to macroscopic phenomena, and are complemented by simplified representations of porous media, such as regular or random sphere packs [8, 9, 10, 11, 12, 13] and physical micromodels [14].

Various computational methods have been developed and applied at pore scale to study flow and transport phenomena [15, 16, 17]. Considering the complexity of the pore geometries, the first step prior to modeling is to characterize the pore space and structures. Imaging techniques such as X-ray microtomography (XMT) [18] and magnetic resonance velocimetry (MRV) measurements [19, 20, 21, 22, 23] have made it possible to obtain accurate 3D characterizations of the pore ge-

ometry at high resolution. Pore-scale modeling can then proceed either by simulating directly on the complex pore geometry, or on a conceptualized pore network that maintains the same topological structure. The first type of model is typically referred to as direct numerical simulation (DNS). DNS approaches include computational fluid dynamics (CFD) [24], Lattice-Boltzmann method (LBM) [25], and smoothed particle hydrodynamics (SPH) [26]. The second type of model represents the pore space as a network connected by stylized pore bodies and pore throats, and most commonly takes the form of pore-network models (PNM) [27]. Both flow and transport processes can be represented using either of these approaches.

Computational fluid dynamics (CFD) techniques use various numerical discretization methods (e.g. finite volume method, finite difference method, etc) to solve the governing partial differential equations (PDEs, e.g. Navier-Stokes equations for incompressible flow). Their use in pore-scale modeling requires generation of a structured or unstructured numerical mesh describing the pore geometry. Smolarkiewicz & Winter [2] applied an implicit immersed-boundary method (IMB) to conduct a series of numerical simulations of the flow through randomly generated media of different porosities. Recently, Yang et al. [1] used finite volume method (FVM) based CFD techniques to solve the Navier-Stokes flow equations on a micro-sized beads pack and successfully compared the pore-scale flow field with magnetic resonance velocimetry (MRV) measurements. These and many other CFD-based pore-scale simulation studies have demonstrated the potential utility of numerical simulations and provided preliminary verification of their equivalence to experimental observations.

The lattice-Boltzmann method (LBM) is a particle-based, modern numerical approach and very well suited for solving the flow since its strength lies however in the ability to easily represent complex physical phenomena in irregular geometries. It has been successfully used in the study of flow in porous media at the pore scale [29]. Pan et al. [30] quantitatively evaluate the capability and accuracy of the LBM for modeling flow through porous media. Three-dimensional flow through a body-centered cubic (BCC) array of spheres and a random-sized sphere-pack were both examined in their study. Their results demonstrate that the Multi-Relaxation-Time (MRT)LBM model is superior to the BhatnagarGrossKrook (BGK)LBM model, and that interpolation significantly improves the accuracy of the fluid-solid boundary conditions. Recently, Khirevich et al. [31] introduced the two-relaxation-times (TRT)-LBM model and thoroughly studied its impact on the accuracy of the drag force/permeability computations with the D3Q19 velocity set in both regular and random packings of monodispersed spheres or cubics.

The Smoothed Particle Hydrodynamics (SPH) method, is a mesh-free Lagrangian particle method first proposed for astrophysical problems by Lucy [32] and Gingold and Monaghan [33] and now widely applied. A key advantage of particle methods such as SPH is in their ability to advect mass with each particle, thus removing the need to explicitly track phase interfaces for problems involving multiple fluid phases or free surface flows. The computational price for managing free particles has been improved by the development of new parallel hardware architectures. In contrast to the LBM, SPH directly solves discretized forms of the PDEs, just as do the CFD techniques. Tartakovsky et al. [4] compared their SPH solution of the diffusion equation with fixed and moving reactive solidfluid boundaries to analytical solutions and LBM simulations. Coupled three-dimensional flow, reactive transport and precipitation in a fracture aperture with a complex geometry were also successfully simulated.

The fourth major pore-scale modeling approach - pore-network method (PNM) - simulates the pore geometry by conceptually interconnecting fundamental units such as pore throats and pore bodies. This method retains the complete topology of a real pore geometry, but does not represent the actual details of the pore structures as required by the other methods. Because the solution of PDEs for the pore network model reduces to simultaneous solution of a set of analytical solutions for flow in each network element, the pore network method is less computationally demanding than the other approaches, and has been successfully applied to a broad range of problem types (e.g., [34, 27]). Mehmani et al. [5] developed a new streamline splitting method (SSM) to more accurately solve the flow and transport system at the pore scale. SSM was verified with direct simulations and validated against micromodel experiments across a wide range of pore-structure and fluid-flow parameters.

Each pore-scale numerical approach mentioned above has strengths in areas such as accuracy, flexibility, computational speed, or scalability. Hence there is a strong benefit in intercomparing these models using benchmark problems. While each of these four methodologies has been widely applied to simulate pore-scale fluid flow and other processes, there have been relatively few systematic comparisons of these different methodologies for a complex representative of real porous media. Oostrom et al. [14] conducted a series of nonreactive solute transport experiments in pore-scale micromodels and offered the data to the pore-scale modeling community to test their numerical simulators. Five pore-scale models and one continuum-scale model were used to simulate the experiments in 2D, including CFD, LBM and PNM. Comparisons between experimental and numerical results for the four challenge experiments show that all pore-scale models were all able

to satisfactorily simulate the experiments. However, comparable studies based on three-dimensional porous geometries have not yet been performed.

Recently, researchers at Montana State University used high-resolution magnetic resonance velocimetry (MRV) to generate three-dimensional images of fluid flow through a randomized bead pack at pore-scale resolution (40 micrometers). The bead pack used for MRV measurements was constructed of 6864 monodispersed polystyrene beads (Duke Scientific, Inc.) with a diameter of $500\mu m$. The MRV results were previously compared with FVM-based CFD models by [1]. The results compared very well spatially, which inspired the extension of these validation studies to include a variety of pore-scale simulation methods, leading to the research reported here. In the current benchmark study, six computational codes embodying the four major pore-scale numerical approaches introduced above (CFD, LBM, SPH and PNM)) have been applied to the same bead pack simulation described in [1] . This paper describes and intercompares the results of flow and solute transport simulations among these four methodologies and with the experimental MRV observations.

The outline of this paper is as follows: 1) the benchmark problem is introduced, including the pore geometry, flow and solute tracer conditions, and information on mesh generation methods; 2) the four major pore-scale numerical approaches are described in greater detail, including three CFD codes (two FVM and one IMB), one LBM code, one PNM code and one SPH code. Information includes descriptions of the governing equations, numerical algorithms, boundary conditions, mesh type and grid resolutions, computing cost and other requirements of each method; 3) results of the simulations are presented in terms of both flow field comparisons (velocities, pressure drop, etc.) and solute transport comparisons (breakthrough curves and dispersion); and 4) a summary of conclusions is provided.

2. Benchmark Problem

The benchmark problem describes flow and non-reactive solute transport through a centimeter-scale column packed with 6864 random monodispersed polystyrene beads (Figure 1). The diameter of the beads is $500\mu m$, and the porosity of the beads pack is 0.4267 as measured by the MRV experiments. However, the modeled porosity is mesh-dependent and varies slightly among the various numerical simulations. The pore geometry used in the various numerical models was specified directly from the voxel data provided in the MRV geometry dataset. The centroids (locations of the beads center) were identified from the voxel data using

an algorithm called Sphere Lociextraction through Iterative Erosion (SLIE, [1]). The dimensions of the beads pack, the flow conditions and boundary conditions for the pore-scale simulations were specified to match the experimental conditions (Table 1). However, for CFD simulations, in order to achieve fully-developed flow at the inlet and outlet faces, two buffer regions were added to the inlet and outlet of the beads pack. For the flow conditions, standard properties of water (density and viscosity) were applied. For the boundary conditions, a fixed volumetric flow rate of $100ml/hr$ ($2.771 \times 10^{-5} kg/s$) was employed at the inlet, consistent with experimental conditions. The outlet boundary is defined as a specified pressure condition. The other surfaces are treated as no-slip boundaries. However, the specific treatment of boundary conditions varies somewhat among the different numerical approaches as described in the next section. The darcy flux, average pore velocity and grain-scale Reynolds number of the experimental system are listed in Table 1, and demonstrate that the flow is in the laminar regime.

Solute transport was not conducted in the MRV experiments, and thus was not simulated in previous work reported by [1]. Accordingly, solute transport simulations performed here can only be compared among the various codes and methods, not with experimental observations. For the numerical simulations reported here, the solute was assumed to have a molecular diffusion coefficient (D_m) of $2.08 \times 10^{-9} m/s^2$, representative of a dilute bromide tracer. The corresponding Schmidt number ($S_c = \frac{\mu}{\rho D_m}$) is 428.3.

Table 1: Dimensions and parameters of the column

Parameter	Symbol (Units)	Value
Length of the column	$L_c(mm)$	16.8
Length of the beads pack	$L_b(mm)$	12.8
Diameter of the column	$D(mm)$	8.8
Diameter of the beads	$d_p(mm)$	0.5
Porosity	ε	0.4267
Volumetric flow rate	$Q(kg/s)$	2.771×10^{-5}
Fluid density	$\rho(kg/m^3)$	997.561
Fluid dynamic viscosity	$\nu(pa-s)$	8.887×10^{-4}
Darcy flux	$q(m/s)$	4.556×10^{-4}
Pore velocity	$v_e(m/s)$	1.068×10^{-3}
Reynolds number	Re_p	0.6
Molecular diffusion coefficient	$D_m(m^2/s)$	2.08×10^{-9}
Schmidt number	Sc	428.3

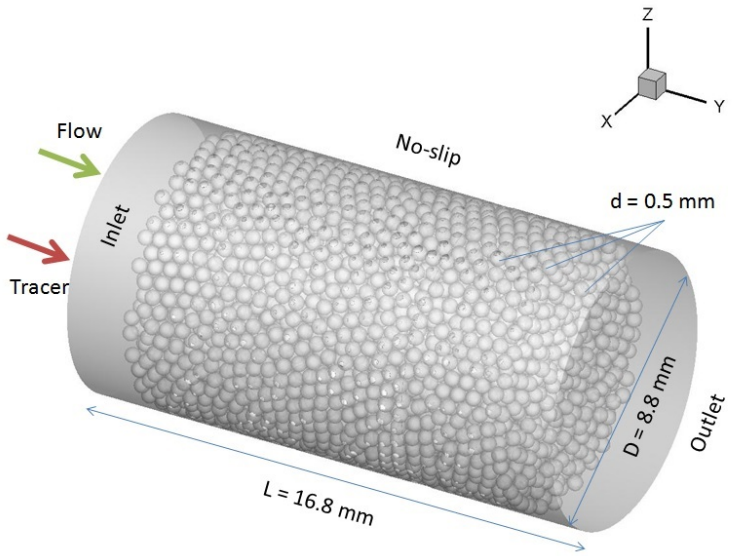

Figure 1: Computational domain of the benchmark beads-pack problem: pore geometry, dimension and boundary conditions.

3. Numerical Model Descriptions

In the current study, we intercompare four major pore-scale numerical approaches that can be divided into two classes: 1) those that explicitly model the three-dimensional geometry of pore spaces and 2) those that conceptualize the pore space as a topologically consistent set of stylized pore bodies and pore throats. Three of the four approaches (CFD, LBM, and SPH) belong to Class 1, and the fourth (PNM) belongs to Class 2. An overview of the six computational codes considered, which implement these four model types, is shown in Table 2, which includes the model names, institution names and numerical methods used to solve governing equations for both the flow and transport processes.

Computational meshes used to represent the complex pore geometry for the numerical simulations were generated in two ways (Figure 2): 1) structured (Cartesian) mesh, and 2) unstructured body-fitted meshes based on the sphere geometry. The direct voxel meshing approach simply uses Cartesian-type mesh elements defined in direct correspondence to the cubic voxel elements output images from the MRV measurement. The images captured using magnetic resonance imaging (MRI) technique were defined using two different resolutions: 20 μm and 40 μm. The same mesh resolutions were used directly in the CFD-TETHYS and LBM

Table 2: Summary of the numerical models

Name of the code	Institution	Numerical method
TETHYS	Pacific Northwest National Laboratory	Finite volume
StarCCM+	CD-adapco	Finite volume
EULAG	University of Arizona	Immersed-boundary
UT-PNM	University of Texas	Pore network
iRMB-LBM	Technische Universität Braunschweig	Lattice Boltzmann
ISPH	Sandia National Laboratories	Smoothed Particle Hydrodynamics

simulations. CFD-IMB simulations are less dependent on the grid resolution (the solid boundaries are simulated by forces). Hence an 80 μm structured mesh was used. The particle-based SPH simulations used 34 μm and 23 μm as their grid resolutions respectively. The STAR-CCM+ code was employed to perform CFD simulations based on an unstructured body-fitted mesh (40 μm as base size) as described in [1].

3.1. Computational Fluid Dynamics (CFD)

CFD applications to pore-scale simulations are often referred as direct numerical simulations (DNS, class 1) because the governing conservation equations (mass and momentum) for laminar flow and the passive scalar equation for transport are solved on a fixed mesh that retains the full pore geometry to the limits of the grid resolution and, for grid-independent solutions, are effectively exact solutions of the Navier-Stokes equations. For the current benchmark problem, three different computational codes/packages were tested: two use FVM and one uses IBM.

3.1.1. TETHYS

The Transient Energy Transport Hydrodynamics Simulator (TETHYS) code, developed at Pacific Northwest National Laboratory, is an applied CFD toolkit for environmental simulations with the capabilities to simulate hydrodynamics, solute transport and reactions. TETHYS uses a finite-volume scheme [35] to discretize the governing equations for conversation of mass, momentum (Navier-Stokes equations) and transported scalars on an unstructured mesh. Previous research using TETHYS includes laminar flow and scalar transport in a tube with sinusoidal-wavy wall [36], 3D pore-scale flow in a beads pack[1] and 3D pore-scale flow and solute transport in a soil column [37].

TETHYS uses the finite volume method (FVM) [38] to discretize the governing PDEs into a system of algebraic equations that are solved using iterative linear

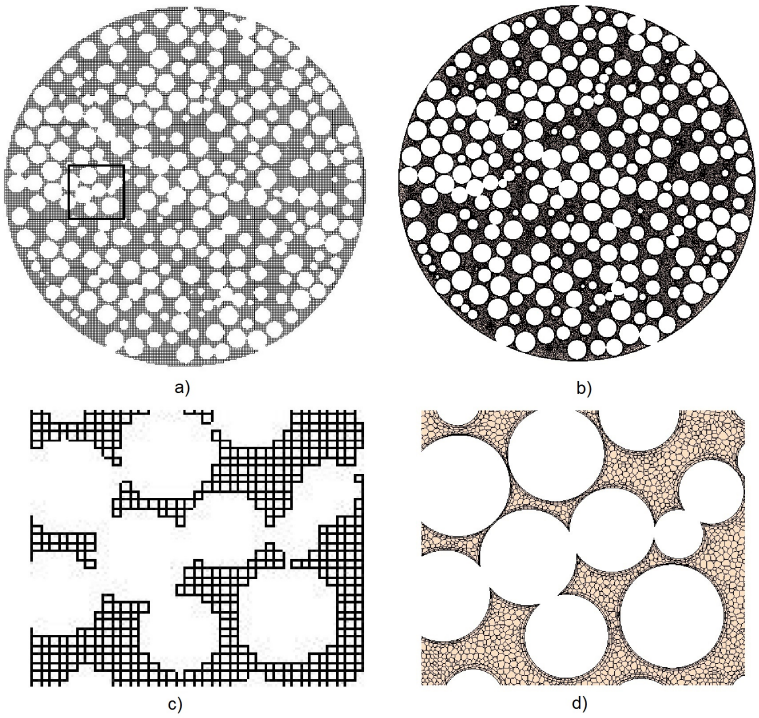

Figure 2: Representative mesh used in the pore-scale simulations (sampled at the selected slice 320 located at the center of the beads pack): a) 40 μm-structured (Cartesian) mesh used in CFD-TETHYS and LBM; b) unstructured body-fitted mesh used in STAR-CCM+; c) and d) are zoomed-in mesh samples from the same location on slice 320.

algebra methods. A segregated solution scheme based on the SIMPLE algorithm [35] is used to solve the flow field [36]. Second-order convection schemes are available for the transport of both momentum and scalars. These are implemented for unstructured meshes using the methods of [39]. In this work, central differencing was used for momentum, and MUSCL for scalar transport. An implicit first-order scheme is used for transport time marching.

Unstructured rectilinear meshes with two resolutions (20 μm, 72.1M cells, and 40 μm, 9.1M cells) were used in TETHYS simulations (Figure 2a,c). For both meshes, a steady hydrodynamic solution was obtained first, then used as a constant flow field for the transport simulation. For hydrodynamics, the boundary conditions used in the TETHYS simulation followed the experimental setup. A constant mass flow rate was imposed at the inlet and a constant pressure was imposed at the outlet. All solid walls were treated as no-slip wall boundaries. The initial conditions were zero velocity and constant pressure. For the transport simulation, the passive scalar value was initially zero everywhere. The inlet concentration was set equal to 1.0 for 2.798 seconds then 0.0 for the rest of the simulation period (50 seconds).

The transport simulations were performed on the Cascade cluster at the Environmental Molecular Sciences Laboratory (EMSL). The transport simulation on the 40 μm mesh used 480 cores for approximately 7 hours. For the 20 μm mesh, the simulation used 1600 cores and took approximately 12 hours.

TETHYS was also used to compute a macroscopic effective axial dispersion coefficient directly using the method of volume averaging (MVA) [40, 41, 42]. Richmond et al. [36] provides a full description of the implementation of MVA in TETHYS and a simple application as validation. To use MVA, the domain of interest must have a periodic boundary in the axial direction. Only the 40 μm mesh was used. The inlet and outlet boundaries were changed to periodic boundaries with the same pressure drop that was produced in the original hydrodynamic simulation. The original hydrodynamic solution was used as initial conditions. After convergence, the resulting flux was the same as specified in the CFD simulation. The MVA calculations converged very slowly for the Peclet number corresponding to the simulated case, and thus were very computationally expensive. The calculation was performed on PNNL's Institutional Computing clusters (Olympus and Constance) using 480 cores and took approximately 5 days to complete.

3.1.2. STAR-CCM+

The commercial software STAR-CCM+ (CD-adapco, Melville, NY, USA) was used to simulate pore-scale flow and transport in the beads pack. Previous

research [1, 14] has demonstrated the advantages and accuracy of using STAR-CCM+ for pore-scale modeling in complex pore geometries. Employing a user-defined automatic sphere generation script implemented in STAR-CCM+, a CAD geometry description of the beads pack was constructed. Then during the embedded mesh generation procedure, the surfaces of the spheres and the pore space were smoothly meshed by polyhedral cells and prism layers (Figure 2b). 7 million polyhedral cells were generated by this approach, which was previously demonstrated to be sufficient based on mesh-independence studies reproted in [1].

Three-dimensional Navier-Stokes equations describing incompressible fluid flow and a passive scalar transport equation at the pore scale are discretized using standard FVM techniques [38] and an algebraic multigrid linear solver. The numerical algorithms include a second-order upwind scheme for convection and diffusion terms, an implicit first-order scheme for time marching and second-order central differencing scheme for the unsteady term. The iterative SIMPLE algorithm is also used to couple the velocity and pressure fields. The convergence criteria is set to be 10^{-6} for continuity.

The boundary conditions, initial conditions and flow/solute transport conditions are the sames as those in TETHYS. The simulations were run in parallel on a DELL workstation T7500 (Intel(R) Xeon(R) CPU, 2.53GHz, 4 processors). The flow field solution was found to converge in about 3000 iterations requiring 15 hours. Upon convergence the flow field was fixed during the solute transport simulation. The time step was 0.01 seconds for the transient passive scalar simulation with 100 inner iterations. The total simulation time was 50 seconds, which required 45 hours of total computing time.

3.1.3. EULAG

Pore-scale simulation requires two key ingredients: a method for prescribing pore space; and a method for representing relevant elements of fluid dynamics. The latter method is technically simple, and advantageous when multiple realizations of a pore spaces are required. EULAG is a multi-scale computational fluid model developed by NCAR, see [43] for a recent review, that has been adapted to simulate flows through porous media in [2]. The adaptation utilizes the the immersed-boundary (IMB) method that employs fictitious body forces in the equations of motion to mimic the presence of solid structures and internal boundaries. The particular technique adapted is a variant of feedback forcing, with implicit time discretization admitting rapid attenuation of the flow to stagnation (within solid structures) in $\mathcal{O}(\Delta t)$ time comparable to the time step Δt of the fluid model.

In EULAG, the governing system of the conservation laws is integrated numerically using a second-order-accurate, semi-implicit, non-oscillatory forward-in-time (NFT) approach, either as Lagrangian evolution equations or Eulerian conservation laws. In this adaptation of EULAG to porous media, all calculations used the Eulerian option in a Cartesian-framework,

The Cartesian model domain is resolved with $N_x \times N_y \times Nz = 128 \times 128 \times 256$ points of the regular grid with uniform intervals $\Delta x = \Delta y = \Delta z = 80\mu m$. In [2] adaptation of EULAG to porous media to support gravity driven flows and simulating flow with through the bead pack with prescribed volumetric flux was achieved by setting the gravity is to $g = 0.049349$ and the kinematic viscosity of that water $\mu = 10^{-6} m^2 s^{-1}$ to simulate flow with the desired Reynolds number ($Re_p = 0.6$).

With the same flow condition setup used in the other CFD simulations, EULAG was programmed in MATLAB and running in a desktop machine (single 3.2 GHz processor). The flow field solution was converged in 300 iterations requiring a simulation time of 4 hours.

3.2. Pore Network Model (PNM)

The University of Texas (UT) group used a pore-network model (PNM) to simulate the flow and transport processes. Pore networks are simplified representations of porous media and are networks of interconnected pores and throats. Often, pores are approximated by spheres and throats by cylinders. It was attempted to honor the real pore geometry of the beads pack as closely as possible. PNM typically assume that pores comprise all the volume of the pore space and that throats solely provide resistance to flow. In real, complex porous media the geometry of each throat in the network is unique. The flow equation is obtained by imposing mass balance at every pore and since the fluid is Newtonian and incompressible, it results in a linear system of equations. Solving this system gives the pressure and velocity fields needed for subsequent solution of the transport equation. The details of this procedure are given by [44].

The PNM simulations of flow and transport in this work were performed using three different Eulerian methods: a) the mixed-cell method (MCM) (e.g. [45, 46], b) the streamline-splitting method (SSM) [5], and c) the superposing transport method (STM) [44, 47]. For more information on these models the reader is additionally referred to a recent review by [48]. In MCM, all the void volume is assigned to the pores and throats are assumed to be volumeless. MCM additionally assumes the solute to be perfectly mixed within pores and ignores the shearing of solute due to non-uniform velocity profiles within throats; the latter referred

to as shear-dispersion hereafter. SSM similarly neglects shear-dispersion within throats, but properly accounts for the partial mixing of solute within pores. In SSM, the void volume is similarly assumed to be concentrated at the pores. On the other hand, STM properly accounts for shear-dispersion within throats, but assumes perfect mixing within pores. In STM, we assume all the void volume to be concentrated at the cylindrically shaped throats, and the pores to be volumeless. STM is by no means limited to this latter assumption, which was made merely out of convenience and to follow common practice in the literature regarding similar Lagrangian network models of transport [47, 48]. In STM, the shearing of the solute within the cylindrical throats is, thus, due to the parabolic velocity profile within them.

For compatibility reasons with the PNM codes used herein, the cylindrical beads-pack column was cropped into a cuboid with the same height in the y-direction, and a square-shaped cross-section with a diameter equal to the column diameter. The pore-network was extracted from the cropped domain using LSU's Avizo module, which employs a techniques outlined in [49]. Briefly, a maximal ball algorithm is used to locate the centers of each pore. Throat hydraulic conductivities are then calculated using methods from [50], whereby irregular throat shapes are mapped onto triangular, square, and circular geometries, depending on their shape factors. A constant pressure gradient was imposed on the pore network in the y-direction to establish steady-state flow and compute the pressure/velocity fields. Solute was then injected through the inlet by imposing a constant inlet concentration of 1 for the duration of 2.798 secs, which was thereafter set to 0 for the rest of the simulation. Zero concentration gradient was imposed at the outlet. Breakthrough profiles (BTP) were obtained by computing the flux-averaged concentrations of all throats at the outlet face of the network. All three methods were implemented in MATLAB and were run on a desktop machine with an Intel Core i7-4790 CPU @ 3.6GHz processor and 32GB of Random Access Memory.

The BTP obtained from SSM is not shown in this paper, as it is almost identical to that of MCM. This is in agreement with the conclusion drawn by [47]: pore-level mixing assumptions have little impact on longitudinal dispersion in disordered granular media. The wall-clock times for the MCM, SSM, and STM simulations were 45 secs, 50 mins, and 3.5 days, respectively. We note that the majority of the difference between the computation times of MCM and SSM were caused by their very different implementations. While the implementation of MCM utilizes heavy vectorization and avoidance of loops, that of SSM does not. On equal grounds, SSM should be roughly twice as costly as MCM. Both MCM and SSM use the adaptive time stepping ode23tb solver in MATLAB, which is an imple-

mentation of TR-BDF2, an implicit Runge-Kutta formula. The relatively higher computational cost of STM, however, is to a larger extent algorithmic. STM solves a non-local (in time) transport equation, which requires pore concentrations to be dynamically recorded during the simulation [47]. This is a memory-intensive process. In addition, STM uses a constant time step throughout the simulation (unlike MCM and SSM). These two factors are the major contributors to STMs higher computational cost. However, practical solutions to considerably alleviate these problems were proposed in [47], the implementation of which will the subject of future work.

3.3. Lattice Boltzmann Method (LBM)

The lattice Boltzmann simulations were performed with the cumulant lattice Boltzmann method [3]. This method uses a finite velocity discretization of the Boltzmann Transport Equation using 27 speeds. The lattice Boltzmann method operates in the hydrodynamic limit of the Boltzmann Transport Equation such that the Navier-Stokes Equation is recovered for small Mach and Knudsen numbers.

The Boltzmann Transport Equation is originally an equation for gaseous flow. In the low Mach number limit gases and liquids usually behave very similar but the flow through a porous medium is an exception to this rule. Due to the high hydrodynamic resistivity of the geometry in the current study a significant pressure drop between inlet and outlet is observed. In a gas this would lead to a compressible flow condition since the density of an isothermal gas is linked to its pressure. As the fluid in the current study is water we have to modify the lattice Boltzmann method such that density and pressure are decoupled [51]. The density of the fluid is enforced to be constant and an incompressible steady state solution is obtained.

The incompressible cumulant lattice Boltzmann method was implemented for parallel execution on General Purpose Graphics Processing Units (GPGPUs) using CUDA. The geometry was discretized with a sparse Cartesian grid using the Eso-Twist data structure [52]. The communication between GPGPUs was done using MPI.

The boundary conditions were constant velocity at the inlet, no-slip at the surface of the spheres and the bounding cylinder and non-reflective extrapolation at the outlet.

Two resolutions were considered. The grid with a resolution of 20 μm contained about 53.5 million nodes while the grid with resolution of 40 μm had about 6.7 million nodes. The case with lower resolution was run on a single TESLA K40c GPGPU requiring 4.5 hours for the flow simulation of about 72 seconds

real time. We achieved a performance of approximately 233.3 million node updates per second (*MNUPS*). The high resolution case was distributed over two K40c and six TESLA C1060 GPGPUs and required $61,07$ hours (2 x K40c GPGPUs) and $66,93$ hours (6 x TESLA C1060 GPGPUs) for the flow simulation of about 72 seconds real time.

3.4. Smoothed Particle Hydrodynamics (SPH)

In this work we use a consistent second-order Incompressible Smoothed Particle Hydrodynamics (ISPH) method [53]. The method is implemented using the massively parallel particle library LAMMPS [54] and the linear algebra library Trilinos [55].

The Smoothed Particle Hydrodynamics (SPH) method is a fully Lagrangian Particle Method for solving conservation equations. Traditionally, incompressible fluids are treated in SPH as weakly compressible fluids and an equation of state is used to close the system of the momentum and continuity equations. The speed of sound, c is chosen so that the Mach number M satisfies the condition $M = \frac{c}{v} \leqslant 0.1$. Under this condition, the compressible fluid behaves as incompressible. Standard SPH discretization is based on the bell-shaped compactly-supported kernel $W(x)$, and represents spatial derivatives of any function in terms of the values of this function at discretization points and derivatives of W. The advantage of standard SPH is that the resulting momentum equations have the form of the equations of Molecular Dynamics, i.e., the SPH descrtization of the continuity, momentum, and advection diffusion equations exactly conserves mass and momentum and, when explicit time integration is used, the SPH algorithms are easily parallelizable. There are two main challenges in application of the weakly-compressible time explicit SPH method to flow in porous media. The accuracy of the standard SPH discretization is hard to control as it depends on the SPH particle distribution. As particles becomes disordered, the convergence rate of SPH method becomes less than two with respect to the resolution parameter, h, the support of W. The second challenge is that the time step in explicit time integration schemes, subject to the CFL conditions, becomes prohibitively small because of the speed of sound and viscosity constraints. A review of the SPH methods with application to pore-scale flows can be found in [56].

The consistent ISPH method uses a splitting scheme to ensure a divergence-free velocity field, which relaxes CFL constraints and allows taking a significantly larger time steps comparing to the weakly compressible SPH. To achieve second order accuracy in time and space, the consistent ISPH method uses an incremental

pressure correction scheme in combination with differential operator renormalization.

SPH simulations with two different resolutions are performed. In these simulations, SPH particles are initially placed on Cartesian mesh with grid sizes 34 μm and 23 μm. SPH particles located inside the beads are labeled as "solid" particles, their positions are fixed in space and they are used to impose the no-slip boundary condition according to the method of [57]. The rest of the particles are labeled as fluid particles, and their positions are advected in time with velocities found from the SPH solution of the Navier-Stokes equations. The periodic boundary condition is used at the top and bottom of the bead pack and the flow is driven by a body force. The initial velocity is set to zero and the NS equations are integrated until steady state average velocity is reached.

The simulations were run on the Hopper supercomputer at the National Energy Research Scientific Computing (NERSC) center using up to 30000 CPUs for the higher resolution simulations. The computing time for flow simulations was approximately 7 hours.

3.5. Summary of the numerical models

A total of four pore-scale models (six computational codes/packages) were used to simulate flow and transport in the benchmark beads pack problem. A summary is given in Table 3, which includes the name of the code, the mesh used in the simulation (mesh type, grid size and number of cells) and computing cost. It is obvious that PNM runs the fastest due to the relative simplicity of the model. On the other hand, the computational cost of the DNS were substantial, with run times up to several days on supercomputers to resolve the more complex problems dealing with high pore-aspect ratios and a flow-focusing heterogeneity. With the implementation of the modern GUGPU technique (CUDA), the computing time could be dramatically shortened, which is concluded from the LBM runs.

4. Results

In this section, we present a series of comparisons for flow and transport among the above mentioned six pore-scale codes/packages. First, simulated velocity fields are evaluated including macroscopic pressure drop and permeability, contour plots of velocities and point-by-point velocity values at selected locations. Second, for the transport simulation, breakthrough curves are presented followed by the dispersion analysis using both analytical solution fitting and volume averaging method [41].

Table 3: Summary of the mesh, grid size and run time *(f: flow; t: transport)

Code	Mesh type	Grid size	No. of Cells	Machine	Run time*
TETHYS	Cartesian	20 μm	72.1M	1600 CPUs	f: 9 hrs
					t: 12 hrs
TETHYS	Cartesian	40 μm	9.1M	480 CPUs	f: 4 hrs
					t: 7 hrs
STAR-CCM+	Polyhedral	40 μm	13M	4 CPUs	f: 15 hrs
					t: 45 hrs
EULAG	Cartesian	80 μm	1.1M	desktop	f: 4 hrs
PNM	–	–	–	desktop	f: 1 s
					t: MCM - 45 s t: SSM - 50 mins t: STM - 3.5 days
LBM	Cartesian	20 μm	53.5M	2 TESLA K40c	f: 61.07 hrs
LBM	Cartesian	40 μm	6.7M	1 TESLA K40c	f: 4.5 hrs
ISPH	Meshless	34 μm	4.8M	30k CPUs	f: 7 hrs

4.1. Flow Field

4.1.1. Pressure drop and permeability

The pressure drop across the bead pack column is an important parameter to evaluate the macroscopic performance of the pore-scale models. In the intercomparisons, the pressure drop is numerically measured by the pressure difference between the inlet and outlet of the column. The expected pressure drop across the uniform sphere packs can be estimated through correlations presented in [58, 59], which gives a value of 14.29 Pa. The pressure drop can also be estimated using the well-known Carman-Kozeny equation [60]. The values of the pressure drop are summarized in Table 4. Using a structured voxel mesh, the corresponding calculated pressure drops from TETHYS simulations were 13.32 Pa (40 μm) and 13.19 Pa (20 μm), respectively, with differences less than 1% compared to the Carman-Kozeny correlation (13.19 Pa) and 4.5% compared to the correlation in [58, 59]. Using the same grid resolutions, pressure drop from LBM simulations were 15.20 Pa and 16.26 Pa, which are slightly higher than those computed from TETHYS. EULAG used a coarser grid resolution (80 μm) and resulted in a higher pressure drop than the other methods (17.13 Pa). The grid resolutions used in SPH simulation was fine enough that the calculated pressure drop was 13.61 Pa with less than 5% difference. The simulated pressure drop for STAR-CCM+ (using unstructured body-fitted mesh) was 13.65 Pa, with a difference of only 4.5%. For Class 2 model-PNM, the pressure drop along the beads pack was 13.26 Pa, which

is also very close to the results from Carmen-Kozeny equation and CFD simulations.

Given the total flux, pressure drop, and column porosity, the permeability associated with each simulation can also be calculated. The permeability of the packed bed, based on the simulated pressure drop for one of the Class 1 model using body-fitted mesh (STAR-CCM+ simulation), is around $4.2 \times 10^{-6} cm^2$ The corresponding estimate from the Class 2 model (PNM) is $4.23 \times 10^{-6} cm^2$, very close to the value simulated by the CFD method. This value is in the typical range observed for clean well-sorted sand. Therefore the simulated macroscopic behavior is consistent with that expected based on established empirical relationships for packed bed systems.

Table 4: Comparison of the pressure drop (ΔP) along the axial direction of the beads pack

Numerical Method	$\Delta P(Pa)$	Error %
[Eisfeld, Reichelt]	14.29	0
Carmen-Kozeny Eq.	13.19	7.7
TETHYS (40 μm)	13.32	6.79
TETHYS (20 μm)	13.19	7.7
EULAG	17.13	19.87
LBM (40 μm)	15.20	6.37
LBM (20 μm)	16.26	13.79
StarCCM+	13.65	4.48
SPH	13.61	4.76
PNM	13.26	7.21

4.1.2. Velocity comparisons

Contour plots of the simulated velocity magnitude along a selected axial slice ($Y = 6.4mm$) in the middle of the bead pack, obtained from all Class 1 pore-scale models, are shown in Figure 3. We find similar flow field patterns in the pore space simulated using different models with either structured or body-fitted mesh. However, due in part to different grid resolutions, the magnitudes of the velocities are not exactly the same. We also note that higher velocities are observed in the near-wall region, where the local porosity is higher than average because of arrangements of the grains associated with the wall effect.

The spatial patterns of velocity are generally in excellent agreement among the different models, but some differences can be noticed in detailed views. Figure 3h shows an expanded view of the subregion of slice 320 indicated by the black box in Figure 3f. Five locations in this subregion (around a pore with high velocity) were

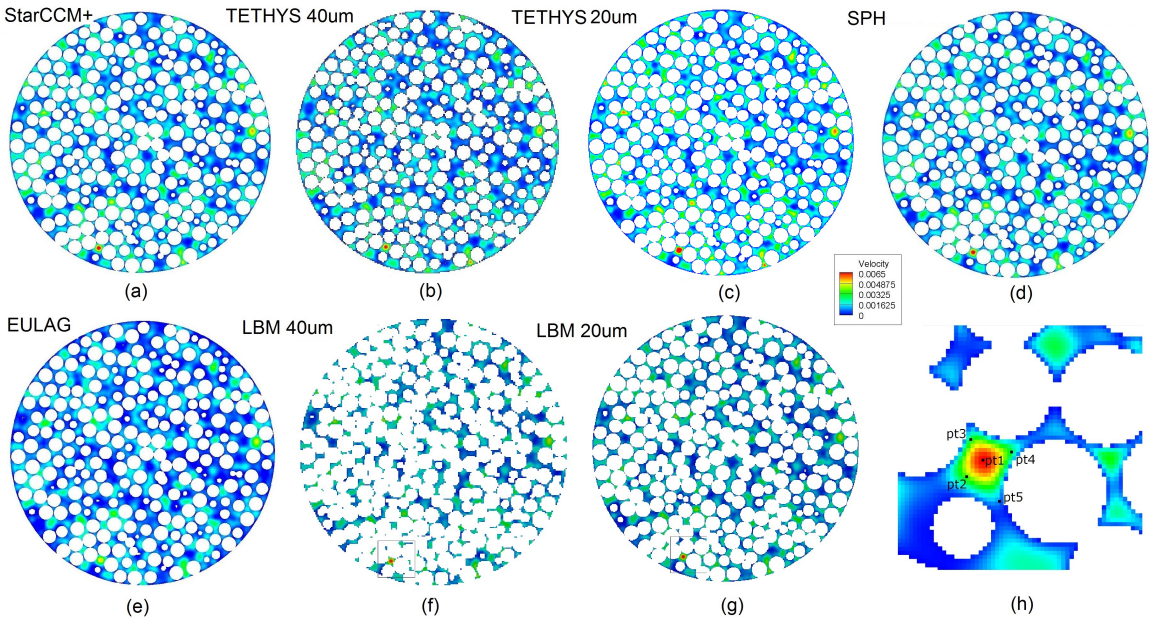

Figure 3: Color contour plots of velocity in slice 320 (in the middle of the packed-bed at Y = 6.4 mm): (a) STAR-CCM+ simulation; (b) TETHYS 40 μm simulation; (c) TETHYS 20 μm simulation; (d) ISPH simulation; (e) LBM 40 μm simulation; (f) LBM 20 μm simulation; (g) EULAG simulation; (h) Magnified visualization of velocity fields in the subregion of slice 320 indicated by a black box in (f) and (g)

selected to compare point-to-point values. Table 5 provides a tabular listing of the actual values of three velocity components (axial and two transverse directions) at all five points. We note that the values predicted by the five different simulation methods are mostly similar, but in selected cases the differences are significant, in particular in those models that employed different grid resolution or mesh type. Results from STAR-CCM+ and ISPH are the closest; we note that both of these methods avoid discrepancies associated with the stair-step mesh geometry used in the other Class 1 methods.

Table 5: Comparison simulated values of axial and transverse velocity components at five selected locations in slice 320 indicated in Figure 4.1.2

	STAR-CCM+	TETHYS		LBM		EULAG	ISPH
		20 μm	40 μm	20 μm	40 μm		
v_y (m/s)							
Point 1	0.007142	0.007038	0.006622	0.008135	0.007834	0.006554	0.007035
Point 2	0.005387	0.005942	0.005667	0.005071	0.004249	0.004728	0.005453
Point 3	0.005186	0.005013	0.004774	0.004299	0.003282	0.004882	0.005213
Point 4	0.00186	0.002042	0.001958	0.003321	0.003238	0.00899	0.00189
Point 5	0.000425	0.000431	0.000407	0.000854	0.001347	0.000357	0.000432
v_x (m/s)							
Point 1	-0.00055	-0.000566	-0.000584	-0.000731	-0.000589	-0.00042	-0.00056
Point 2	-0.000542	-0.000539	-0.000514	-0.000252	-0.00027	-0.00039	-0.000548
Point 3	-0.000636	-0.000641	-0.000622	-0.000722	-0.000347	-0.000547	-0.000642
Point 4	-0.000096	-0.000094	-0.000102	-0.000186	-0.000146	-0.00088	-0.000092
Point 5	0.000088	0.000093	0.000090	0.000071	0.00005	0.000043	0.000084
v_z (m/s)							
Point 1	-0.000182	-0.000185	-0.000177	-0.002234	-0.002223	-0.000172	-0.000179
Point 2	-0.000148	-0.000143	-0.000139	-0.001897	-0.001668	-0.000131	-0.000145
Point 3	-0.000097	-0.000110	-0.000110	-0.001304	-0.001202	-0.000082	-0.000096
Point 4	-0.000942	-0.000931	-0.000906	-0.000946	-0.000741	-0.000756	-0.000947
Point 5	-0.000634	-0.000592	-0.000682	-0.000587	-0.000864	-0.000423	-0.000659

4.2. Solute Transport

4.2.1. Breakthrough curves

In this section, computed results for solute transport are presented and compared between CFD and PNM simulations. Figure 4 shows three-dimensional visualizations of tracer concentration in the beads pack at four selected times (t = 5, 15, 25, and 35 seconds), which were simulated by TETHYS (Class 1 CFD-FVM). For the solute transport simulations (based on converged steady-state flow solution), we imposed a pulse-type constant concentration at the inlet of the column

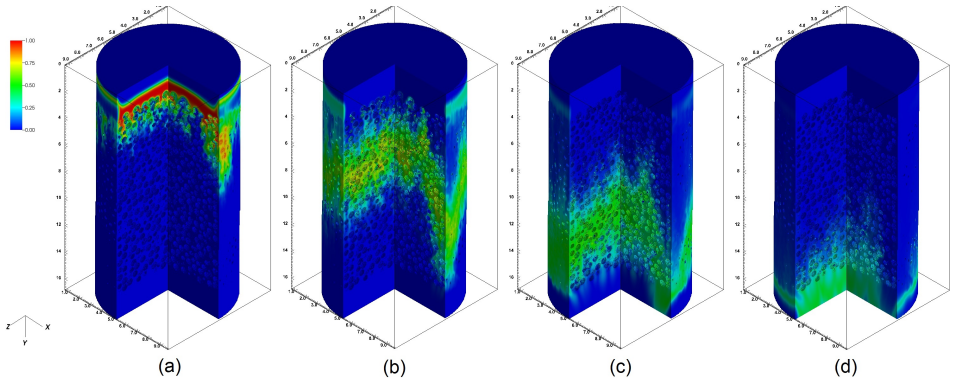

Figure 4: Visualizations of tracer concentration at four selected simulation times: (a) 5 s; (b) 15 s; (c) 25 s; (d) 35 s.

for 2.78 seconds then kept it as zero for the rest of the simulation period. Therefore the highest concentrations occur in the early stages of the transport simulation (Figure 4a). By using pressure boundary condition at the outlet, we made sure that the solute would exit eventually (Figure 4d). From those images, it is clear that the pore geometry has a major impact on the character of the transport simulation. It is evident that there is strong preferential flow along the column walls, which is an artifact that would not occur in the natural system. In the absence of this wall effect, the overall flow rate and effective hydraulic conductivity would be smaller, and the tracer breakthrough would occur later.

Figure 5b shows the contour plot of the solute concentration on the selected slice 320 at time = 10 seconds. By comparing with the velocity magnitude contour plot (Figure 5a), it is clear that solute trapping occurs in lower-velocity regions, which are towards the central part of the beads pack. This trapped tracer can be expected to lead to extended tailing in the corresponding breakthrough curve.

Figure 6 shows simulated breakthrough curves at the inlet and outlet of the beads pack column for the bromide tracer. Three pore-scale models were used to simulate solute transport based on the flow field solutions. At the inlet, we employed a pulse-type incoming concentration (duration = 2.78 seconds) as denoted in the figure. At the outlet, breakthrough concentrations were calculated from the simulation results using a flux-weighted average at each time step. The breakthrough curve results are consistent with the interpretations drawn from the visualizations (Figure 4). In particular, the long extended tailing in the breakthrough curves reflect the trapping of solute in low-advection regions. The peak of the breakthrough curves appear at around 22 seconds, which includes the time

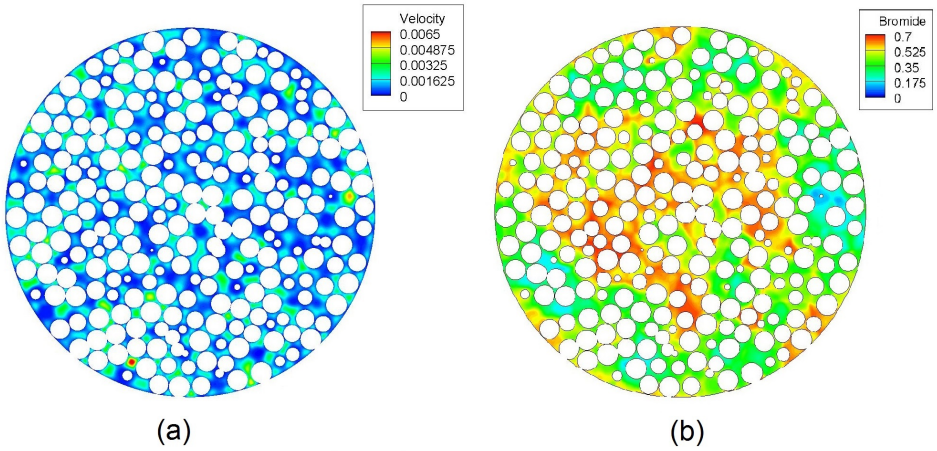

Figure 5: Contour plots of velocity (left image) and tracer concentration at time = 10 s (right image) in slice 320.

for the solute traveling through the extruded buffer regions added to the beads pack. The breakthrough curves computed from TETHYS using both 40 μm and 20 μm structured mesh are very close to each other and to the results from STAR-CCM+ using the unstructured body-fitted mesh. However, the breakthrough curve simulated using the Class 2 model - PNM - shows some discrepancies from the Class 1 models. Since the PNM did not include the buffer regions, we ran a comparable STAR-CCM+ simulation without the buffer regions for a more relevant comparison as shown in (Figure 6). From this comparison, it can be seen that the initial arrival and rising limb of the breakthrough curves are very similar between the two methods, but the PNM method appears to be more dispersive in nature, leading to a lower peak and longer tail. This difference may be in part due to the cropping of the column edges to create the cubic domain for PNM; the edges of the model domain have generally faster velocities due to the edge effects therefore leading to apparently longer travel times when only the central part of the domain is considered. Further analyses are being conducted to determine the cause of this discrepancy between the models.

4.2.2. Dispersion analysis

The macroscopic longitudinal dispersion coefficient can be estimated from the simulations for comparison. Here we used to methods to estimate dispersion. For the simulation methods that performed transport simulations, the resulting breakthrough curves were fitted with a standard one-dimensional advection-dispersion

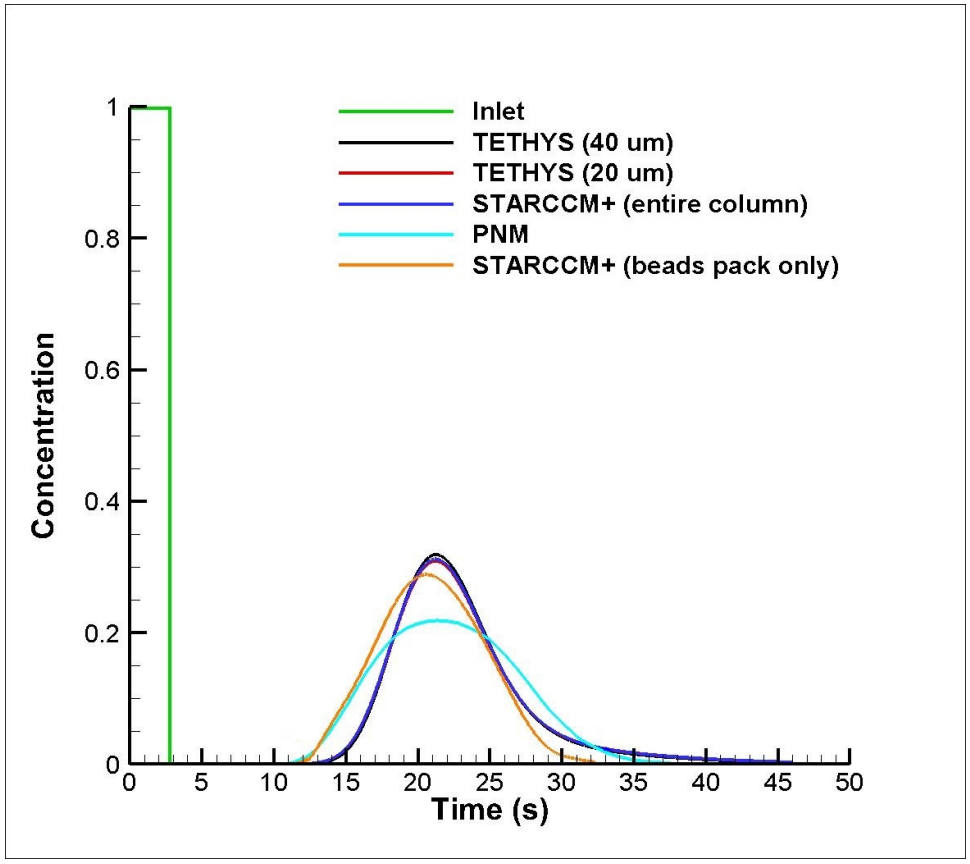

Figure 6: Computed breakthrough curves (concentration of solute tracer over time) at the outlet of the column.

model using the STAMMT-L code. We also used the method of volume averaging (MVA), solved numerically using the TETHYS code, to obtain estimates of dispersion coefficients corresponding to the simulated system. Richmond et al. [36] modified the MVA that it could be applied to unsteady cases. The modified MVA has been previously validated for the simple cases of flow between parallel plates and tubes, and was subsequently applied to a sinusoidal wavy tube problem and successfully compared with transport simulations based on a particle tracking method [36].

The results of the MVA analysis for a range of normalized Pe numbers ($Pe = Sc \times Re$, from 0.1 to 1000) are presented in Figure 7. The calculated Pe number of the current beads pack problem is 257 ($Pe* = 110$). The estimated dispersion coefficients based on fitting of the simulated breakthrough curves are also shown in Figure 6. The results show very good agreement between the modified MVA method and the values fitted to the 1D advection-dispersion equation.

5. Conclusions

We have performed comparative simulations of an experimental porous medium using six different codes representing four general pore-scale modeling approaches. The methods vary widely in the degree of complexity of representation of the porous media geometry, the numerical algorithms used, mesh resolution and geometry, and computational requirements. Quantitative comparisons are drawn in terms of microscopic measures (pore-scale velocities) and macroscopic measures (permeability, breakthrough curves, effective dispersivity). All models and codes gave broadly similar results in all categories, although there were some differences that may be deemed significant depending on the model context.

In particular, the EULAG implementation of the Immersed Boundary Method and the Lattice Boltzmann Method implementation both led to a smaller effective permeability (larger pressure drop) for the mini-column than the other CFD methods that had been previously validated against the experimental measurements. Comparisons of simulated tracer breakthrough were only performed for a subset of the codes considered, but illustrated some differences between the CFD methods (which were consistent with each other) and the PNM method, which matched the early breakthrough closely but led to a lower peak concentration and longer late arrival tail (i.e., larger apparent dispersivity).

The computational demands of the various methods also varied widely, with some methods running in minutes on a single processor and others requiring hours or days on large supercomputers. The PNM in particular is highly computationally

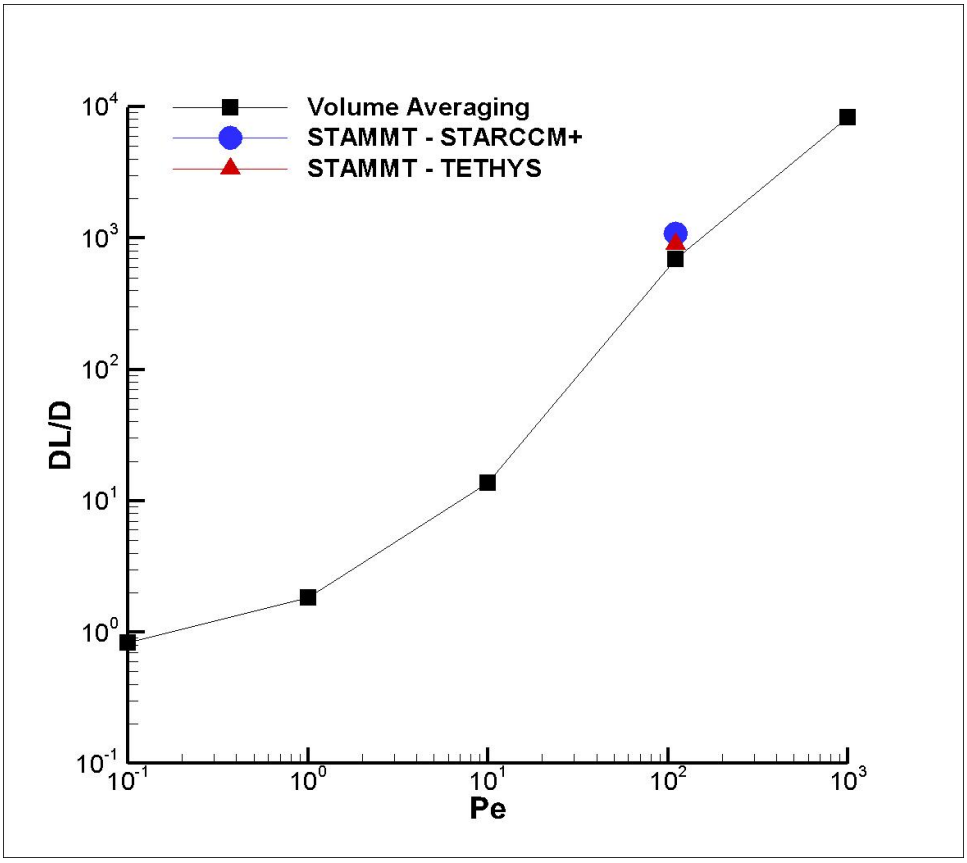

Figure 7: Computed axial dispersion coefficients.

efficient, and therefore may be very well suited to rapid screening of alternatives or performing very large simulations in cases where modest overestimation of dispersive transport is not problematic.

Additional analyses are needed to clearly identify the sources of the observed discrepancies, and further work is needed to enhance code capabilities to allow common comparison of transport simulations across the full suite of methods. However, in general we believe that this study provides a strong foundation for further development and application of pore-scale simulation methods to problems of porous media flow and transport.

6. Acknowledgments

Research at Pacific Northwest National Laboratory (PNNL) was supported by the U. S. Department of Energy (DOE) Office of Biological and Environmental Research (BER) through the PNNL Subsurface Biogeochemical Research Scientific Focus Area project. Computations described here were performed using computational facilities of the Environmental Molecular Sciences Laboratory (EMSL), a national scientific user facility sponsored by DOE-BER and located at PNNL, computational facilities of PNNL's Institutional Computing program, and computational facilities of the National Energy Research Supercomputing Center, which is supported by the DOE Office of Science under Contract No. DE-AC02-05CH11231. PNNL is operated for the DOE by Battelle Memorial Institute under Contract No. DE-AC06-76RLO 1830.

The pore network modeling was carried out under funding from the Center for Frontiers of Subsurface Energy Security, an Energy Frontier Research Center funded by the U.S. Department of Energy, Office of Science, and Office of Basic Energy Sciences, DOE Project No. DE-SC0001114. We would also like to thank Karsten Thompson and LSU for providing the network extraction algorithm to develop the pore network models.

Sandia National Laboratories is a multiprogram laboratory managed and operated by Sandia Corporation, a wholly owned subsidiary of Lockheed Martin Corporation, for the U.S. Department of Energys National Nuclear Security Administration under contract DE-AC04-94AL85000. This SPH work was supported by the DOE Office of Science Advanced Scientific Computing Research (ASCR) Applied Mathematics program as part of the Collaboratory on Mathematics for Mesoscopic Modeling of Materials (CM4). This research used resources of the National Energy Research Scientific Computing Center, a DOE Office of Science User Facility supported by the Office of Science of the U.S. Department of Energy under Contract No. DE-AC02-05CH11231.

[1] X. F. Yang, T. D. Scheibe, M. C. Richmond, W. A. Perkins, S. J. Vogt, S. L. Codd, J. D. Seymour, M. I. McKinley, Direct numerical simulation of pore-scale flow in a bead pack: Comparison with magnetic resonance imaging observations, Advances in Water Resources 54 (2013) 228–241.

[2] P. K. Smolarkiewicz, C. L. Winter, Pores resolving simulation of darcy flows, Journal of Computational Physics 229 (9) (2010) 3121–3133.

[3] M. Geier, M. Schonherr, A. Pasquali, M. Krafczyk, The cumulant lattice boltzmann equation in three dimensions: theory and validation, Computers & Mathematics with Applications accepted.

[4] A. M. Tartakovsky, P. Meakin, T. D. Scheibe, R. M. E. West, Simulations of reactive transport and precipitation with smoothed particle hydrodynamics, Journal of Computational Physics 222 (2) (2007) 654–672.

[5] Y. Mehmani, M. Oostrom, M. T. Balhoff, A streamline splitting pore-network approach for computationally inexpensive and accurate simulation of transport in porous media, Water Resources Research 50 (3) (2014) 2488–2517.

[6] J. Bear, Dynamics of Fluids in Porous Media, Dover Publications, Inc., New York, 1972.

[7] J. Bear, A. H.-D. Cheng, Modeling Groundwater Flow and Contaminant Transport, 1st Edition, Vol. 23 of Theory and Applications of Transport in Porous Media, Springer Netherlands, 2010.

[8] T. Suekane, Y. Yokouchi, S. Hirai, Inertial flow structures in a simple-packed bed of spheres, Aiche Journal 49 (1) (2003) 10–17.

[9] M. Nijemeisland, A. G. Dixon, Cfd study of fluid flow and wall heat transfer in a fixed bed of spheres, Aiche Journal 50 (5) (2004) 906–921.

[10] P. R. Gunjal, V. V. Ranade, R. V. Chaudhari, Computational study of a single-phase flow in packed beds of spheres, Aiche Journal 51 (2) (2005) 365–378.

[11] R. S. Maier, D. M. Kroll, R. S. Bernard, S. E. Howington, J. F. Peters, H. T. Davis, Enhanced dispersion in cylindrical packed beds, Philosophical Transactions of the Royal Society of London Series a-Mathematical Physical and Engineering Sciences 360 (1792) (2002) 497–506.

[12] R. S. Maier, D. M. Kroll, R. S. Bernard, S. E. Howington, J. F. Peters, H. T. Davis, Hydrodynamic dispersion in confined packed beds, Physics of Fluids 15 (12) (2003) 3795–3815.

[13] R. S. Maier, M. R. Schure, J. P. Gage, J. D. Seymour, Sensitivity of pore-scale dispersion to the construction of random bead packs, Water Resources Research 44 (6).

[14] M. Oostrom, Y. Mehmani, P. Romero-Gomez, Y. Tang, H. Liu, H. Yoon, Q. Kang, V. Joekar-Niasar, M. T. Balhoff, T. Dewers, G. D. Tartakovsky, E. A. Leist, N. J. Hess, W. A. Perkins, C. L. Rakowski, M. C. Richmond, J. A. Serkowski, C. J. Werth, A. J. Valocchi, T. W. Wietsma, C. Zhang, Pore-scale and continuum simulations of solute transport micromodel benchmark experiments, Computational Geosciences (2014) 1–23.

[15] P. H. Valvatne, M. Piri, X. Lopez, M. J. Blunt, Predictive pore-scale modeling of single and multiphase flow, Transport in Porous Media 58 (1-2) (2005) 23–41.

[16] Y. Zaretskiy, S. Geiger, K. Sorbie, M. Forster, Efficient flow and transport simulations in reconstructed 3d pore geometries, Advances in Water Resources 33 (12) (2010) 1508–1516.

[17] A. M. Tartakovsky, P. Meakin, T. D. Scheibe, B. D. Wood, A smoothed particle hydrodynamics model for reactive transport and mineral precipitation in porous and fractured porous media, Water Resources Research 43 (5), w05437.

[18] D. Wildenschild, A. P. Sheppard, X-ray imaging and analysis techniques for quantifying pore-scale structure and processes in subsurface porous medium systems, Advances in Water Resources 51 (2013) 217–246.

[19] J. D. Seymour, P. T. Callaghan, Generalized approach to nmr analysis of flow and dispersion in porous media, Aiche Journal 43 (8) (1997) 2096–2111.

[20] J. D. Seymour, S. L. Codd, E. L. Gjersing, P. S. Stewart, Magnetic resonance microscopy of biofilm structure and impact on transport in a capillary bioreactor, Journal of Magnetic Resonance 167 (2) (2004) 322–327.

[21] J. D. Seymour, J. P. Gage, S. L. Codd, R. Gerlach, Anomalous fluid transport in porous media induced by biofilm growth, Physical Review Letters 93 (19).

[22] J. D. Seymour, J. P. Gage, S. L. Codd, R. Gerlach, Magnetic resonance microscopy of biofouling induced scale dependent transport in porous media, Advances in Water Resources 30 (6-7) (2007) 1408–1420.

[23] C. J. Elkins, M. T. Alley, Magnetic resonance velocimetry: applications of magnetic resonance imaging in the measurement of fluid motion, Experiments in Fluids 43 (6) (2007) 823–858.

[24] J. D. Anderson, Computational Fluid Dynamics, 1st Edition, Mcgraw Hill Series in Mechanical Engineering, McGraw-Hill Science/Engineering/Math, 1995.

[25] S. Chen, G. D. Doolen, Lattice boltzmann method for fluid flows, Annual Review of Fluid Mechanics 30 (1998) 329–364.

[26] J. J. Monaghan, Smoothed particle hydrodynamics, Annual Review of Astronomy and Astrophysics 30 (1992) 543–574.

[27] B. Bijeljic, M. J. Blunt, Pore-scale modeling of transverse dispersion in porous media, Water Resources Research 43 (12).

[28] T. Yiallourou, L. Asboth, J.-R. Kroeger, D. Maintz, A. C. Bunck, N. Stergiopulos, B. A. Martin, Quantitative comparison of 4d mri flow measurements to 3d computational fluid dynamics simulation of cerebrospinal fluid movement in the spinal subarachnoid space, in: 10th International Workshop on Biomedical Engineering, IEEE, 2011, pp. 1–4.

[29] M. C. Sukop, H. Huang, C. L. Lin, M. D. Deo, K. Oh, J. D. Miller, Distribution of multiphase fluids in porous media: Comparison between lattice boltzmann modeling and micro-x-ray tomography, Physical Review E 77 (2).

[30] C. X. Pan, L. S. Luo, C. T. Miller, An evaluation of lattice boltzmann schemes for porous medium flow simulation, Computers & Fluids 35 (8-9) (2006) 898–909.

[31] S. Khirevich, I. Ginzburg, U. Tallarek, Coarse- and fine-grid numerical behavior of mrt/trt lattice-boltzmann schemes in regular and random sphere packings, Journal of Computational Physics 281 (2015) 708–742.

[32] L. B. Lucy, A numerical approach to the testing of the fission hypothesis, Astronomical Journal 82 (1977) 1013–1024.

[33] R. A. Gingold, J. J. Monaghan, Smoothed particle hydrodynamics - theory and application to non-spherical stars, Monthly Notices of the Royal Astronomical Society 181 (2) (1977) 375–389.

[34] H. Dong, M. J. Blunt, Pore-network extraction from micro-computerized-tomography images, Physical Review E 80 (3).

[35] S. V. Patankar, Numerical Heat Transfer and Fluid Flow, Hemisphere, Washington, DC, 1980.

[36] M. C. Richmond, W. A. Perkins, T. D. Scheibe, A. Lambert, B. D. Wood, Flow and axial dispersion in a sinusoidal-walled tube: Effects of inertial and unsteady flows, Advances in Water Resources 62 (2013) 215–226.

[37] T. D. Scheibe, W. A. Perkins, M. C. Richmond, M. I. McKinley, P. D. J. Romero-Gomez, M. Oostrom, T. W. Wietsma, J. A. Serkowski, J. M. Zachara, Pore-scale and multiscale numerical simulation of flow and transport in a laboratory-scale column, Water Resources Research 51 (2) (2015) 1023–1035.

[38] J. H. Ferziger, M. Peric, Computational Methods for Fluid Dynamics, 3rd Edition, Springer-Verlag, Berlin, 2001.

[39] M. S. Darwish, F. Moukalled, Tvd schemes for unstructured grids, International Journal of Heat and Mass Transfer 46 (4) (2003) 599–611.

[40] R. G. Carbonell, S. Whitaker, Dispersion in pulsed systems .2. theoretical developments for passive dispersion in porous-media, Chemical Engineering Science 38 (11) (1983) 1795–1802.

[41] S. Whitaker, The Method of Volume Averaging, Kluwer Academic Publishers, 1999.

[42] B. D. Wood, Inertial effects in dispersion in porous media, Water Resources Research 43 (12) (2007) W12S16.

[43] P. K. Smolarkiewicz, P. Charbonneau, Eulag, a computational model for multiscale flows: An mhd extension, Journal of Computational Physics 236 (2013) 608–623.

[44] Y. Mehmani, Modeling single-phase flow and solute transport across scales, Ph.D. thesis, Petroleum and Geosystems Engineering (2014).

[45] R. C. Acharya, S. Van der Zee, A. Leijnse, Transport modeling of nonlinearly adsorbing solutes in physically heterogeneous pore networks, Water Resources Research 41 (2).

[46] Y. Mehmani, T. Sun, M. T. Balhoff, P. Eichhubl, S. Bryant, Multiblock pore-scale modeling and upscaling of reactive transport: Application to carbon sequestration, Transport in Porous Media 95 (2) (2012) 305–326.

[47] Y. Mehmani, M. T. Balhoff, Pore-network modeling of longitudinal dispersion, Water Resources Research in preparation.

[48] Y. Mehmani, M. T. Balhoff, Mesoscale and hybrid models of fluid flow and solute transport, Reviews in Minerology and Geochemistry in press.

[49] K. E. Thompson, C. S. Willson, C. D. White, S. L. Nyman, J. P. Bhattacharya, A. H. Reed, Application of a new grain-based reconstruction algorithm to microtomography images for quantitative characterization and flow modeling, Spe Journal 13 (2) (2008) 164–176.

[50] T. W. Patzek, D. B. Silin, Shape factor and hydraulic conductance in noncircular capillaries i. one-phase creeping flow, Journal of Colloid and Interface Science 236 (2) (2001) 295–304.

[51] X. Y. He, L. S. Luo, Theory of the lattice boltzmann method: From the boltzmann equation to the lattice boltzmann equation, Physical Review E 56 (6) (1997) 6811–6817.

[52] J. Linxweiler, Ein integrierter softwareansatz zur interaktiven exploration und steuerung von straungssimulationen auf many-core-architekturen (in german), Ph.D. thesis, Institut fr rechnergesttzte Modellierung im Bauingenieurwesen (2011).

[53] N. Trask, M. Maxey, K. Kim, M. Perego, M. L. Parks, K. Yang, J. Xu, A scalable consistent second-order sph solver for unsteady low reynolds number flows, Computer Methods in Applied Mechanics and Engineering 289 (0) (2015) 155–178.

[54] S. Plimpton, Fast parallel algorithms for short-range molecular dynamics, Journal of Computational Physics 117 (1) (1995) 1–19.

[55] M. A. Heroux, R. A. Bartlett, V. E. Howle, R. J. Hoekstra, J. J. Hu, T. G. Kolda, R. B. Lehoucq, K. R. Long, R. P. Pawlowski, E. T. Phipps, A. G. Salinger, H. K. Thornquist, R. S. Tuminaro, J. M. Willenbring, A. Williams, K. S. Stanley, An overview of the trilinos project, ACM Trans. Math. Softw. 31 (3) (2005) 397–423.

[56] A. Tartakovsky, N. Trask, K. Pan, B. Jones, W. Pan, J. Williams, Smoothed particle hydrodynamics and its applications for multiphase flow and reactive transport in porous media, Computational Geosciences (2015) 1–28.

[57] D. W. Holmes, J. R. Williams, P. Tilke, Smooth particle hydrodynamics simulations of low reynolds number flows through porous media, International Journal for Numerical and Analytical Methods in Geomechanics 35 (4) (2011) 419–437.

[58] B. Eisfeld, K. Schnitzlein, The influence of confining walls on the pressure drop in packed beds, Chemical Engineering Science 56 (14) (2001) 4321–4329.

[59] W. Reichelt, Calculation of pressure-drop in spherical and cylindrical packings for single-phase flow, Chemie Ingenieur Technik 44 (18) (1972) 1068–1073.

[60] P. C. Carman, Fluid flow through granular beds, Transactions of the Institution of Chemical Engineers 15 (1937) 150–166.